Journal of Materials Research and Technology 30 (2024) 2125–2139

Contents lists available at ScienceDirect

Journal of Materials Research and Technology

journal homepage: www.elsevier.com/locate/jmrt

Discrete model for discontinuous dynamic recrystallisation applied to grain structure evolution inside adiabatic shear bands

Elijah Borodin [a,*], Oleg Bushuev [a], Vladimir Bratov [b], Andrey P. Jivkov [a]

[a] Department of Solids and Structures, School of Engineering, The University of Manchester, Manchester M13 9PL, UK
[b] Edinburgh Napier University, Edinburgh EH10 5DT, UK

ARTICLE INFO

Keywords:
Discontinuous dynamic recrystallisation
Adiabatic shear bands
Aluminium alloys
High strain rates
Polytopal cell complex
FEM

ABSTRACT

Discontinuous dynamic recrystallisation (DDRX) is a well-known phenomenon playing a significant role in the high-temperature processing of metals, including industrial forming and severe plastic deformations. The ongoing discussion on the Zener–Hollomon (Z–H) parameter as a descriptor of materials' propensity to DDRX and a measure of microstructure homogeneity leaves more questions than answers and prevents its practical application. Most of the existing DDRX models are continuous, and so the geometry and topology of real grain microstructures cannot be considered. The present study uses a fully discrete representation of polycrystalline aluminium alloys as 2D/3D Voronoi space tessellations corresponding to EBSD maps. Such tessellations are geometric realisations of combinatorial structures referred to as polytopal cell complexes. Combining discrete models with FEM LS-Dyna simulations of shock-wave propagation in AA1050 and AW5083 aluminium alloys makes it possible to estimate for the first time the contribution of DDRX to the final material microstructure inside adiabatic shear bands. It is shown that the increase of the initial fraction of high-angle grain boundaries, caused by preliminary deformation, significantly increases the spatial homogeneity and decreases the clustering of DDRX grains. The obtained results contradict the conventional assumption that the microstructures obtained by severe plastic deformation under quasi-static and dynamic deformation conditions are similar due to the similar value of the Z–H parameter: competition between the two recrystallisation mechanisms leads to almost unpredictable final grain structures inside share bands that require further comprehensive experimental studies. This agrees with experimental evidence for high material sensitivity to the Z–H parameter.

1. Introduction

Workability is a key concept in material forming [1,2] coupling the contributions from external material loading routes and internal microstructure evolution. The effect of loading is traditionally better modelled, and the commonly used finite element analysis (FEA) can provide reliable simulation results [3], especially if the models are supplemented by additional microstructural data [4]. The effect of microstructure evolution is harder to predict in a wide range of strains and strain rates. Further understanding of the micro-mechanisms acting during hot deformation processing is essential for successful incorporation of meso-scale physical models for microstructure evolution into the industrially relevant simulation software.

Capturing plastic flow instabilities is the most challenging element in modelling microstructure evolution. These commonly appear as localisation shear bands — undesirable phenomena in industrial material processing [1,2,5,6]. Shear bands development naturally affects the homogeneity of the material's microstructure and is intrinsically related to the processes of local energy redistribution and accumulation [1,2]. A high level of heterogeneity can be beneficial in some processes [5] but usually the localisation is a precursor for material failure [5,7–9].

While criteria for shear bands initiation have been proposed and validated [9–13], the analysis of their development, involving a complex grain structure evolution within the bands, appears to be a much more complicated task. Dynamic recrystallisation (DRX) [12,14,15] is a key process responsible for the meso-scale structure evolution inside shear bands, leading to a local increase of 2–3 times yield strength [10–12] and the corresponding few times reduction in the material elongation to failure. The inability to manage effectively the DRX process is a critical problem for targeted material design.

Two different DRX mechanisms can be distinguished [14]: continuous dynamic recrystallisation (CDRX) and discontinuous dynamic recrystallisation (DDRX). CDRX consists of the initial formation of a fine sub-grain structure of dislocation walls and low-angle grain boundaries (LAGBs). This stage is followed by sub-grain rotations, leading to an increase in the fraction of high-angle grain boundaries (HAGBs) and

* Corresponding author.
E-mail address: elijah.borodin@manchester.ac.uk (Elijah Borodin).

https://doi.org/10.1016/j.jmrt.2024.03.206
Received 24 November 2023; Accepted 26 March 2024
Available online 1 April 2024

List of the used abbreviations and model variables

ASB	Adiabatic shear bands
DRX	Dynamic recrystallisation
DDRX	Discontinuous dynamic recrystallisation
CDRX	Continuous dynamic recrystallisation
PDRX	Post-dynamic recrystallisation
HAGBs	High-angle grain boundaries
LAGBs	Low-angle grain boundaries
NAG	Nucleation and growth models
SPD	Severe plastic deformation
FEM	Finite element method
EBSD	Electron backscatter diffraction
SHPB	Split-Hopkinson pressure bars
GB	Grain boundary
TJ	Triple junction
QP	Quadruple point
PCC	Polytopal cell complex
$\mathcal{T}$	Tessellation of a 2D or 3D space by polytopes
$\mathcal{M}$	PCC based on a tessellation $\mathcal{T}$
p, p_0	Observed and initial fractions of HAGBs
J_ω	Triple junction ω-types
j_ω	Fraction of ω-type TJs in a PCC
S_J	TJ configuration entropy of HAGBs
B_L	Grain boundary index of HAGBs
W_b^k,	Topological weight of kth grain boundary
n	Number of DDRX grains
κ	Fraction of DDRX grains
η_k	Probability for nucleation of a new DDRX grain on the kth grain boundary
γ_k	Fraction of neighbouring grains containing $k \in \{0,1,2\}$ DDRX grains
ω	Grain clustering index
ρ_D	An average scalar dislocation density
T	Temperature
t	Time
$\dot{\varepsilon}_{pl}$	Plastic strain rate

smaller grains [16,17]. CDRX is typical for many low-temperature deformation processes in aluminium and copper alloys [14,16,18]. In contrast, DDRX strongly depends on thermal instabilities and becomes possible only at relatively high homologous temperatures [14,19].

During DDRX new grain nuclei emerge at pre-existing defect sites, such as grain boundaries (GB) [20,21], and then the nuclei growth by migration of newly formed GBs. When the nucleation rate is higher than the grain growth rate, the average grain size decreases significantly. Recrystallised grains can be detected experimentally in EBSD maps [1] as they are covered with HAGBs and often form the so-called necklace structures [19,22]. The fraction χ (either the volume χ_v or surface χ_s fraction) of recrystallised grains can be measured using SEM and EBSD scans [1]. A few studies report the evolution of the recrystallised grain fraction with time $\chi(t)$ or with accumulated plastic strain $\chi(\varepsilon)$ [23,24].

At quasistatic deformation conditions, the dynamic recrystallisation of SPD-processed metals is a wide and relatively well-developed research area [25–29], including a large body of experimental [16,18,26] and theoretical [25,30] studies. Typically, the incorporation of DDRX models into numerical simulations is attempted by the introduction of several simplifications and parameters requiring empirical fitting. Several continuous and discrete models have been proposed to describe the DDRX process and to estimate the changes in the average grain size [20,31–38], as well as to relate this size to the Zenner–Hollomon parameter [21,22,24,39]. However, the changes in the topological and statistical characteristics of the grain and grain-boundary networks during DDRX have not been considered to date.

With increasing strain rates, materials become unable to transfer the heat generated by the plastic deformation effectively and the shear bands start overheating. In such case, they are referred to as adiabatic shear bands (ASB). ASBs are typically observed during cutting, forming and penetration processes [10,12]. The CDRX mechanism typical for low strain rate SPD processing of aluminium alloys changes to DDRX during plastic deformation, [14] and this transition dramatically affects materials' yield strength and fracture behaviour. The ability to predict this transition and simulate DDRX-caused grain structure refining inside ASB in a wide range of strain rates is critical for large-scale modelling of metal processing.

The present study advanced previous approaches to the simulation of DDRX based on the Monte-Carlo probabilistic methods [20,31,40] and more recent cellular automaton methods implemented on 2-dimension lattices [21,37,38]. The theoretical and numerical models proposed in this work are a step towards a more realistic 3-dimensional model for DDRX that considers explicitly the geometry and topology of the polycrystalline structure. A similar algebraic approach has already been successfully employed to describe the CDRX process during SPD of copper alloys [41–44]. It uses a discrete representation of an initial microstructure of dislocation cells which evolves gradually into a structure of smaller grains bounded by HAGBs. The mathematical structure describing a polycrystalline material is a polytopal cell complex (PCC) – a concept taken from algebraic topology [45] – which is the key tool for analysis and simulation. In the CDRX case, the size and topology of a cell/grain structure remain roughly the same during the recrystallisation process, so the whole CDRX process can be simulated by creating new HAGBs on the elements of a pre-existing sub-grain structure [42–44]. In contrast, during the DDRX process, the nucleation of new grains is an essential part which cannot be neglected. It is technically challenging and requires time-consuming re-tessellation of the initial material's model alongside the recalculation of a new PCC on each calculation step. The new approach presented in Section 2 overcomes these difficulties. The simulation framework is developed using a Python-based DDRX module [46] a part of the Voronoi PCC Analyser code [47], working in conjunction with the free software Neper [48]. It implements the procedure of re-tessellation and recreation of the updated PCCs as described in Section 2.1.

An essential part of the methodology is the mapping of purely structural characteristics of a new grain microstructure, which appears as new polyhedrons in the tessellation and new cells in the corresponding PCC, to the real process variables at time t and accumulated plastic strain ε_{pl}. In this step a physical model for the grain nucleation rate as a function of temperature [33] is employed as described in Section 2.3. In the last two Sections 3 and 4 the contribution of the DDRX process to grain structure evolution in significantly overheated regions inside adiabatic shear bands (ASB) [5,49] is studied numerically for the aluminium of technical purity and 5083 aluminium alloys widely used in the automotive and marine industries [50].

For estimations of average temperature and cooling rate inside ASB in several dynamically loaded aluminium alloys, FEM LS-Dyna [51] simulations are performed as discussed in Section 3. The application of the physical model for DDRX nucleation rate [33] alongside the developed in Section 2.1 discrete methodology and software tools [47] allow for the first time to analyse numerically the spatial distribution of the DDRX-related microstructural characteristics inside ASB.

2. Discrete probabilistic DDRX model

The construction of a DDRX model requires two essential procedures: (i) generation of a combinatorial structure independent of the

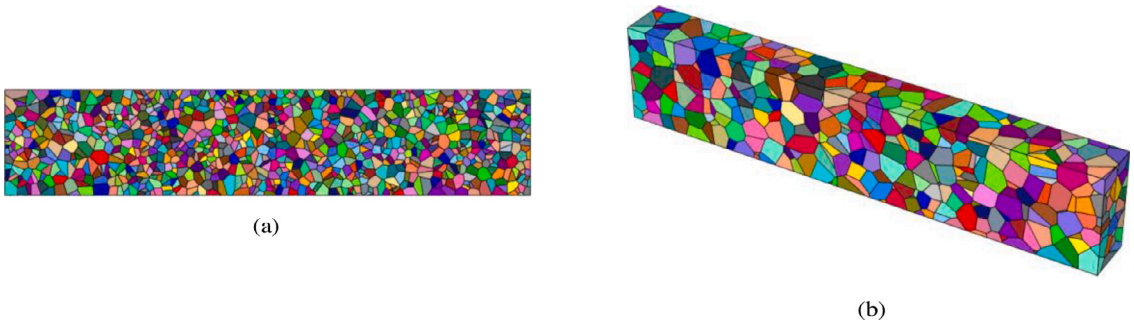

Fig. 1. Voronoi tessellations of (a) two-dimensional and (b) three-dimensional domains.

physical process parameters; and (ii) mapping of combinatorial variables such as fractions of cells to the physical variables of plastic strain, temperature and time. Step (i) creates a realistic discrete representation of a material's microstructure incorporating an initial grain boundary structure at the start of the DDRX process. The effect of the initial grain boundary structure on the DDRX is an important subject of our study demonstrating advantages of the developed discrete algebraic representation over the continuous ones. This part of the model, considering only the interaction effects between the internal substructures of dynamically recrystallised grains and HAGBs, is described in the following Section 2.1. Mapping of structural characteristics, such as defect fractions, to the plastic strain and time variables, is required for simulations of real recrystallisation processes inside ASB observed in dynamic experiments. Such a mapping with corresponding temperature-dependent kinetic equations is described in Section 2.3.

2.1. Structural DDRX model

2.1.1. Space tessellations and related polytopal cell complexes

We consider representations of polycrystalline material's microstructures as polytopal cell complexes (PCC) [43,52–54]. For 3-dimension space tessellation $\mathcal{T}$ the corresponding PCC is a collection of: (1) convex polyhedrons referred to as *3-cells* and representing grains; (2) polyhedral faces, which are convex polygons, referred to as *2-cells* and representing grain boundaries (GBs); (3) polygonal edges, which are line segments, referred to as *1-cells* and representing triple lines/junctions (TJs); and (4) meeting points of edges (corners of polygons and polyhedrons) referred to as *0-cells* and representing quadruple points (QPs). In the 2D case, a PCC is a collection of: (1) convex polygons referred to as 2-cells and representing cuts through volumetric grains; (2) polygonal edges referred to as 1-cells and representing cuts through grain boundaries; and (3) meeting points of edges (corners of polygons) referred to as 0-cells and representing cuts through triple lines.

The construction of a PCC is a two-step process. In the first step, a geometric representation of a polycrystalline microstructure is created by tessellation of a given domain with convex polytopes. This representation is denoted by $\mathcal{T}$. For metals and ceramics realistic $\mathcal{T}$ can be achieved by Voronoi tessellations of space [48,55]. Fig. 1 shows Voronoi tessellations of 2D and 3D domains created by Neper software [48].

In the second step, an algebraic representation of $\mathcal{T}$, denoted by $\mathcal{M}$, is created. This representation is a set of adjacency or incidence matrices [45]. An open-source code Voronoi PCC Analyser [47] is used for the construction of $\mathcal{M}$ based on the Neper output files. The set of incidence matrices can be used to obtain any necessary information about the neighbourhood, boundaries and co-boundaries [52] of the k-cells of $\mathcal{M}$, for $k \in \{0,1,2,3\}$ in 3D and $k \in \{0,1,2\}$ in 2D.

2.1.2. Initial defect structure

The arrangement formed by *special* 3-cells or 2-cells of a PCC associated, respectively, with DDRX grains and HAGBs, is referred to as the defect *structure* [43,44]. Technically, it can be implemented by assigning labels to the elements of $\mathcal{M}$. For example, the GBs represented by 2-cells in $\mathcal{M}$ can be divided into two types — special HAGBs, and ordinary LAGBs [42–44]. In such case, the grains represented by 3-cells in $\mathcal{M}$ can also be considered of two types — special, where grains are fully bounded by HAGBs, and ordinary in all other cases. The fraction of HAGBs, p, is the ratio of the number of special 2-cells, S_2, and the total number of 2-cells in $\mathcal{M}$, N_2 [43]:

$$p = \frac{S_2}{N_2}. \tag{1}$$

Similarly, the fraction of DDRX grains κ, is the ratio of the number of special 3-cells (recrystallised grains), S_3, and the total number of 3-cells in $\mathcal{M}$, N_3:

$$\kappa = \frac{S_3}{N_3}. \tag{2}$$

The fraction of DDRX grains is a key characteristic, which is measured experimentally together with the volume fraction of recrystallised grains $\chi_p = V_{DRX}/V_{all}$ [24], where V_{DRX} is the volume of all DDRX grains and V_{all} is the total volume of the sample. The volume fraction is commonly measured in experimental studies of processed metals. It does not grow significantly when a large number of very small recrystallised grains appear locally inside a small cluster of grains. In contrast, κ would grow fast during such a development. All structural characteristics can be plotted against both fractions κ and χ_p.

The presence of special 2-cells creates a structure in the set of 1-cells of $\mathcal{M}$ representing TJs. For the considered binary classification of GBs as special and ordinary, the TJs are classified into four types J_ω for $\omega \in \{0,1,2,3\}$, where the index gives the number of special GBs meeting at the TJ [43,44,56]. If the number of TJs of type J_ω is denoted by g_ω, and the total number of 1-cells in $\mathcal{M}$ is N_1, then the fractions of the four TJ types are:

$$j_\omega = \frac{g_\omega}{N_1} \tag{3}$$

The initial microstructure before the onset of DDRX can vary and strongly depend on the pre-processing history of a material. In the 2D case, the initial microstructure can be obtained directly from EBSD data using grain barycentres and crystallographic orientations. The corresponding Voronoi tessellation, the PCC, and the substructure of special 2-cells (HAGBs) can be obtained by the PCC Analyser code [47]. A similar approach can be followed for 3D microstructures when 3D EBSD data is available. When such data is not available, 3D microstructures can be created synthetically. In particular, it has been recently shown that HAGBs structure with realistic j_ω distribution – similar to the ones observed in SPD processed alloys – can be obtained by a grain rotation mechanism [42].

The evolution process studied in this work starts with the initial microstructures that do not contain DRX grains, i.e., $\kappa_0 = 0$. These have distributed special 2-cells representing HAGBs and are created by the PCC Processing Design code [57], which is freely distributed as a part of the MATERiA project [55], and allows for generating realistic initial defect microstructures using the grain rotations mechanism [42]. Two different initial fractions of HAGBs will be considered in the work: $p_0 = 0.05$ and $p_0 = 0.25$. In the latter case, it has been assumed that the DDRX starts after the end of preliminary CDRX structure evolution dominated in experiments up to plastic strain $\varepsilon_{pl} \approx 1$ [16].

2.1.3. Nucleation of new grains during DDRX

The challenge in the discrete simulation of the DDRX process comes from the need to repeat the whole two-stage process of domain tessellation and PCC creation many times. This is a computationally expensive procedure, especially in the 3D case. For instance, a typical experimental 2D EBSD scan contains about 5000 grains and 15,000 GBs which corresponds to a 2D section of a 3D cube containing about 373,000 grains with several millions of GBs. Operation with such an amount of data cannot be handled on a desktop computer. At the same time, PCCs with a small number of cells, e.g., 1000, may not be statistically representative. For this work, an initial PCC with 3000 3-cells was used for 3D simulations. The PCCs after the recrystallisation simulations contained up to 60,000 3-cells.

The proposed model uses a kinetic approach to DDRX avoiding complex dynamic simulations of grain growth due to grain boundary migration [58,59]. The tessellation and the creation of $\mathcal{M}$ are repeated after a calculation step, Δt, during which a number of grains could be nucleated and grown. This means that Δt includes both the average nucleation time, τ_n, and the grain growth time, τ_g. The grains created during one calculation step grow independently, but the nuclei of grains in the subsequent step may appear on any grain boundary, including on the boundaries of grains created in the previous step. The number of grains generated in each simulation step is a process-dependent parameter related to the DDRX rate. This number of independently and simultaneously growing grains, Δn_g, can be estimated as $\sim \tau_g/\tau_n$ and must be greater than 1. A constant value $\Delta n_g = N_g/10$ is used in the calculations. This corresponds to the assumption that the grain growth time τ_g is much smaller than the nucleation time τ_n and so most of the grains created in the previous computation step affect the nucleation of the newly created ones. The key feature distinguishing the proposed DDRX model from all continuous approaches is the possibility to select nucleation sites for all Δn_g new grain nuclei at each simulation step. Moreover, a pre-existing HAGB structure and spatial distribution of HAGBs formed during preliminary simulation steps can be explicitly taken into account.

The propensity of a GB for local instabilities, such as nucleation of new grains, is determined by the presence of local stress concentrators created by the GB neighbourhood. Structural indices of GBs have been recently introduced to characterise local stress concentrations [17]. Let α, β, and γ denote the number of 1-cells on the boundary of a 2-cell of types J_1, J_2 and J_3, respectively. The local GB index, characterising the concentration of internal stresses around a GB, is defined by [17]:

$$B_L = \alpha + 2\beta + 3\gamma. \tag{4}$$

For normalising the GB indices B_L so that their values are less than or equal to 1, a topological weight of a cell [54] can be employed. The weight of each 2-cell W_b is the number of its 2-cell neighbours. It allows

The nucleation of new grains becomes increasingly unlikely on GBs with sizes approaching the size of a grain nucleus. This critical size has been taken to be $\delta = 5$ nm. The area of a GB sets a local length scale l_k, equal to the diameter of a disc with the same area. When l_k of a given GB approaches the critical size δ, the probability of grain nucleation on that GB must tends to zero. The probability η_k for nucleation of a new DDRX grain on the kth GB is given by

$$\eta_k = \eta_0 \cdot \frac{2B_L^k}{3W_b^k}\left(1 - \left(\frac{\delta}{l_k}\right)^3\right), \tag{5}$$

where η_0 is a constant nucleation probability for a particular GB type in a stress-free homogeneous material. It can be selected differently for LAGB and HAGB types, such that $\eta_0[LAGB] \ll \eta_0[HAGB]$. In the limit case when $\eta_0[HAGB] = 1$ and $\eta_0[LAGB] = 0$ nucleation of new grains is possible only on HAGBs.

After selecting Δn_g GBs as the sites for nucleation of new grains, it is necessary to select Δn_g points within these GBs as centres of grain nuclei. These points are selected at random with uniform probability inside each of the GB areas. The coordinates of the selected points $\{x_i, y_i, z_i\}$ are added to the list of grain barycentres for the next tessellation stage. During the tessellation stage, the PCC Analyser code [47] determines the new lists of GBs and TJs with their types. HAGBs or LAGBs from the previous simulation step, which have been nucleation sites for new grains, can either remain in the new cell complex or disappear depending on the tessellation. The 2-cells on the boundaries of the newly created grains are considered to be HAGBs. All the other information about the existing HAGBs and DDRX grains is inherited from the previous calculation step.

The proposed approach does not consider nuclei inside grain volumes. It was widely observed in experiments [21,31,37,38] that their number is much smaller than the number of nuclei on GBs. They can be a significant factor only in alloys with a large concentration of precipitates and relatively large average initial grain sizes. In that case, additional experimental data about the spatial distribution of defects would be required.

2.1.4. Structural measures

The final step in the formulation of the structural part of the DDRX model is the calculation of structural characteristics or measures for microstructural states at each simulation step. In addition to the fraction of DDRX grains κ, the fraction of HAGBs p, and the fractions of TJs j_i, let us use the *grain clustering index* ω [56], and the *TJ configuration entropy* S_J [43,44,60]. For materials characterisation tasks, it is important to know what are the relative contributions of DDRX and CDRX mechanisms to these structural measures during the SPD process.

The first characteristic $\omega(\kappa)$ shows the existence of inhomogeneities in the spatial distribution of recrystallised grains. It has been introduced in [56] and employed for the characterisation of cell structure evolution in cubic lattices. This parameter is applicable only for the characterisation of structures where each cell has precisely one neighbour that is the case for grains where each pair share only one common GB.

Consider all the pairs of neighbouring 2-cells in 2D or 3-cells in 3D and denote by γ_k the fraction of such pairs of grains with $k \in \{0, 1, 2\}$ recrystallised DDRX grains. The random distribution of γ_k is well-known [56]:

$$\gamma_{r0} = (1-\kappa)^2, \quad \gamma_{r1} = 2(1-\kappa)\kappa, \quad \gamma_{r2} = \kappa^2, \tag{6}$$

By definition, the sum $\gamma_0 + \gamma_1 + \gamma_2 = 1$. The deviation of a real γ_k distribution from the random case (6) can be expressed by the grain clustering index $\omega(\kappa)$ as [56]:

$$\omega = \begin{cases} 1 - \frac{\gamma_1}{\gamma_{r1}}, & \text{if } \frac{\gamma_1}{\gamma_{r1}} \le 1. \\ \frac{\gamma_0\gamma_2}{\gamma_{r0}\gamma_{r2}}, & \text{if } \frac{\gamma_1}{\gamma_{r1}} > 1. \end{cases} \tag{7}$$

Highly segregated structures have $\omega \to 1$ [56] corresponding to necklace-like clustering of grains covered by HAGBs — typical for DDRX mechanism of recrystallisation. Oppositely, a highly separated structure has $\omega \to -1$ [56], which is more typical for the CDRX mechanism [44].

The clustering of the DRX grain is related to the average grain size of the material, widely used in the Hall–Petch strain hardening law [41]. The grain size in the areas of intense recrystallisation can be very small tending to the size of the new grain nuclea D, while the untouched by the DDRX areas have grain size close to the average initial grain size

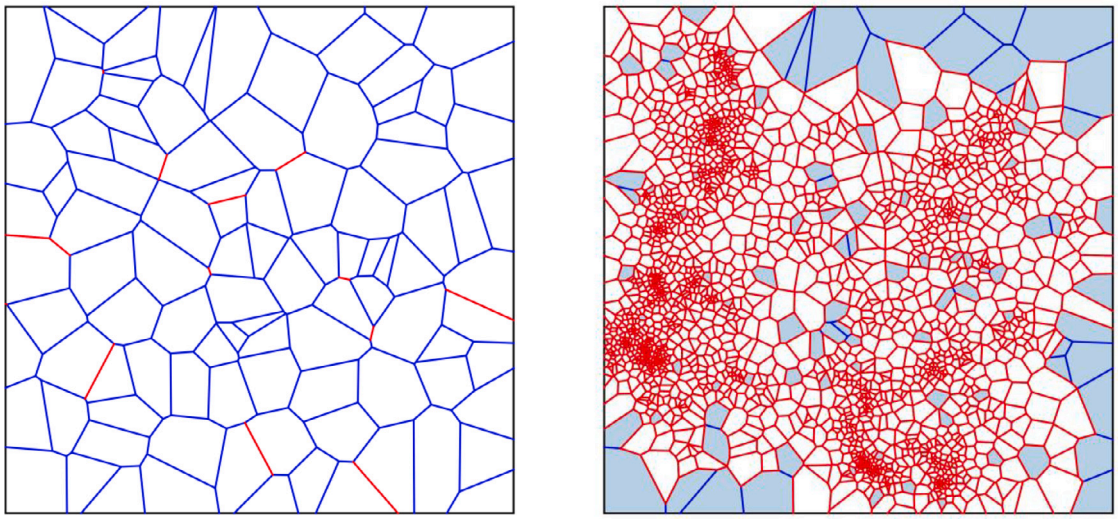

(a) (b)

Fig. 2. Simulation of DDRX process on a 2D structure: (a) initial subgrain structure with 5% HAGBs shown in red; and (b) final grain structure where initial grains unaffected by DDRX are shown in grey.

of material d. Using the compound law, an average grain size at such a bi-modal distribution caused by DDRX can be estimated as:

$$d_{DRX} = \omega \cdot D + (1 - \omega) \cdot d. \tag{8}$$

The essential model assumption, in agreement with the large set of experimental data [14], is that the DDRX grains are fully bounded by HAGBs, which means large differences between their crystallographic orientations and the orientations of their neighbouring grains. Therefore, both fractions of DDRX grains κ and HAGBs fraction p gradually increase during the DDRX process approaching one. The number of calculation steps can be chosen arbitrarily, but it is limited by the maximum desired HAGB fraction $p \approx 1$.

The second characteristic, configuration entropy $S_J(p)$, is based on the TJ types

$$S_J(p) = -(j_0 \cdot log_2 j_0 + j_1 \cdot log_2 j_1 + j_2 \cdot log_2 j_2 + j_3 \cdot log_2 j_3), \tag{9}$$

which depend on the HAGBs fraction p. It was introduced in [60], then independently for SPD processes in [43] and used for structural characterisation and design purposes in [17,42,44]. The configuration entropy is analogous to the Shannon informational entropy [61], and measures the information content stored inside a material. It is a non-monotonous function of p with maximum achieved at $p = 0.5$.

2.2. Changes of structural measures during DDRX

The structural part of the developed DDRX model allows for calculating the changes of the structural characteristics with the growth in the recrystallised grain fraction κ during the deformation process. The results depend on the topology of the material's microstructure, initial spatial distribution and fraction of HAGBs (obtained as the result of a preliminary deformation process), and the principle for selecting grain nucleation sites. However, the structural part does not link to the dynamic (time-dependent) characteristics of the process. Therefore, the results for structure evolution as a function of κ during DDRX can be reused many times for different experimental functions $\kappa(t)$ or $\kappa(\varepsilon_{pl})$ depending on the temperature history. This observation will be used in Section 4.

After the initial generation of a PCC and initialising all the variables, the PCC Analyser code [47] loops over simulation steps and rebuilds the tessellation and the corresponding PCC. In particular, at each iteration step the code:

1. Generates new random seed coordinates and appends them to the file containing all grain seeds in the tessellation $\mathcal{T}$;
2. Creates a new tessellation $\mathcal{T}'$ (by Neper software in 3D) based on the updated grain seed file, and then calculates matrices of the corresponding updated PCC $\mathcal{M}'$;
3. Identifies special grain boundaries and sets them in the new complex $\mathcal{M}'$ inheriting all the HAGBs microstructure from the previous iteration step and the PCC $\mathcal{M}$;
4. Calculates structural measures, including κ, p, j_i, ω and S_J,

until the desired maximum fraction of DRX grains $\kappa \approx 1$ is reached.

For the 2D case, two initial 2D Voronoi tessellations of a square domain containing 100 and 1000 grains and the corresponding PCCs were used. The size of these complexes increases at each calculation step approaching at large fractions of $\kappa \approx 1$ 1878 and 13,506 grains, respectively. The small 100-grain complex was used mainly for visualisation purposes, while the structural characteristics were calculated for the more statistically representative PCC containing initially 1000 grains. In the 3D case, an initial Voronoi tessellation of the elongated 3-dimensional domain (see Fig. 5) and the corresponding PCC containing 3000 grains was used for all simulations. For a large fraction of κ the number of grains grew 18 times up to the recrystallised PCC containing 58,617 grains.

2.2.1. Two-dimensional structure evolution during DDRX

While 2D tessellations with a small number of grains suit well for visualisation of the recrystallisation process and testing of the developed DDRX models, it needs to be recognised that the structure evolution in 3D is more complex and qualitatively different from the 2D case. Therefore, the following figures should be considered only as visualisation tools. Fig. 2 show the initial (Fig. 2(a)) and final (Fig. 2(b)) grain microstructures after 200 calculation steps. The HAGBs are shown in red in both figures. Initially, only 14 GBs (5% of all GBs) were assigned here as HAGBs. The initial grains, which remained unaffected by the DDRX process are filled grey in Fig. 2(b), while the new DRX grains are filled white.

Even in such a small area, the DDRX process is highly localised creating several centres clusters and "islands" of material untouched by the localisation process. The initial spatial distribution of HAGBs contributes significantly even for the small initial fraction of HAGBs $p_0 = 0.05$ as shown in Fig. 3.

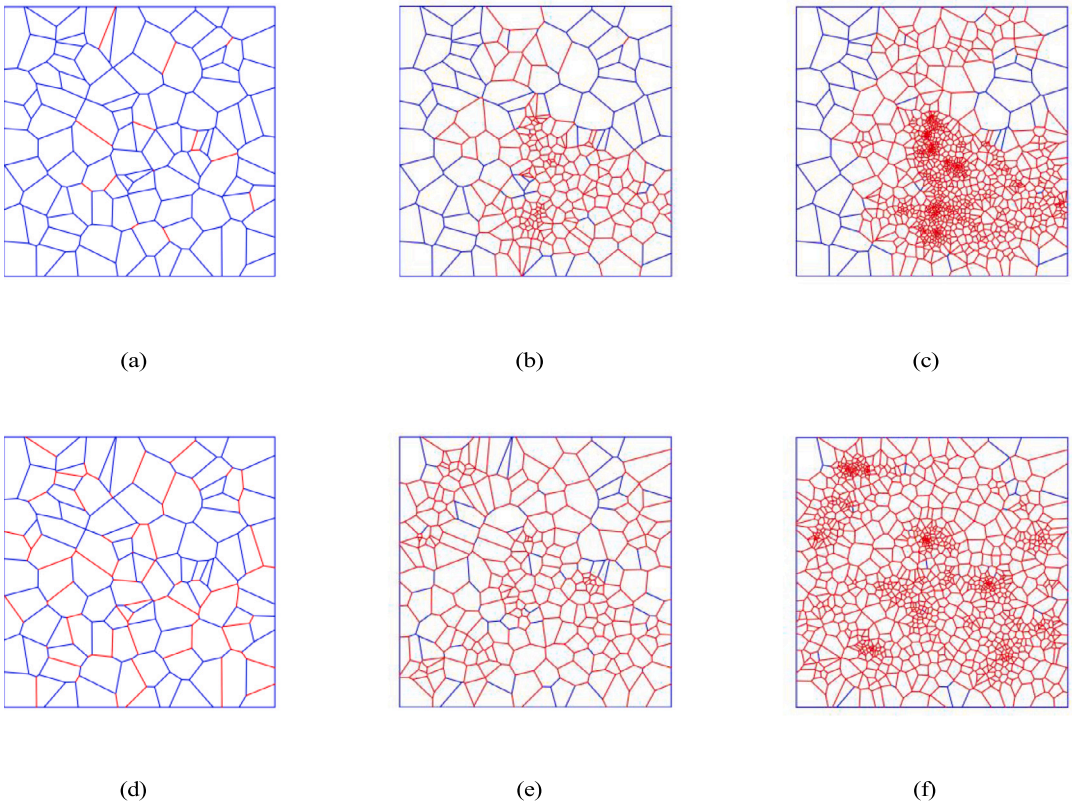

Fig. 3. Evolution of structures with different initial HAGBs densities: starting with (a) $p_0 = 0.05$, then changing as (b) $p = 0.52$, (c) $p = 0.9$; and starting with (d) $p_0 = 0.1$, then changing as (e) $p = 0.52$, (f) $p = 0.9$. HAGBs are shown in red.

In the EBSD scans the DDRX grains are well-known for forming necklace structures [14,19]. Large-scale simulations representing the formation of such patterns require time-consuming computing of large 3D structures containing hundreds of thousands of polytopes. However, even the obtained 2D structures resembling parts of such "necklaces" show a considerable part of material unaffected by the recrystallisation process. More simulation examples are shown on the MATERiA project web page [62]. The source Python code for DDRX simulation based on the 2D/3D Voronoi tessellations and the corresponding PCCs is freely available from the PRISB project repository on GitHub [46].

Fig. 4 shows the evolution of the clustering index ω with the DDRX grain fraction κ at different initial fractions of randomly distributed HAGBs p (5%, 10%, and 30%). By its definition (see Eq. (7)), it can vary in the range $\omega \in [-1, 1]$, where 1 indicating highly segregated grain structure, and -1 indicating chess-like homogeneous spatial distribution of DDRX grains [56]. It is important to mention that in statistically not representative cases, like the appearance of just a couple of DRX grains, it is potentially possible to have $\omega \gg 1$, but these cases have no statistical meaning and should be neglected. At the same time, it causes a problem for small complexes containing a few hundred grains — where even several DRX grains correspond to a notable fraction of κ.

The clustering characterised by ω, clearly decreases with increasing initial fraction of HAGBs. The same tendency is demonstrated in Fig. 3 where the larger initial fraction of HAGBs leads to a more homogeneous distribution of DDRX grains. It will be shown that the same relation between ω and the initial fraction of HAGBs remains in the 3D case.

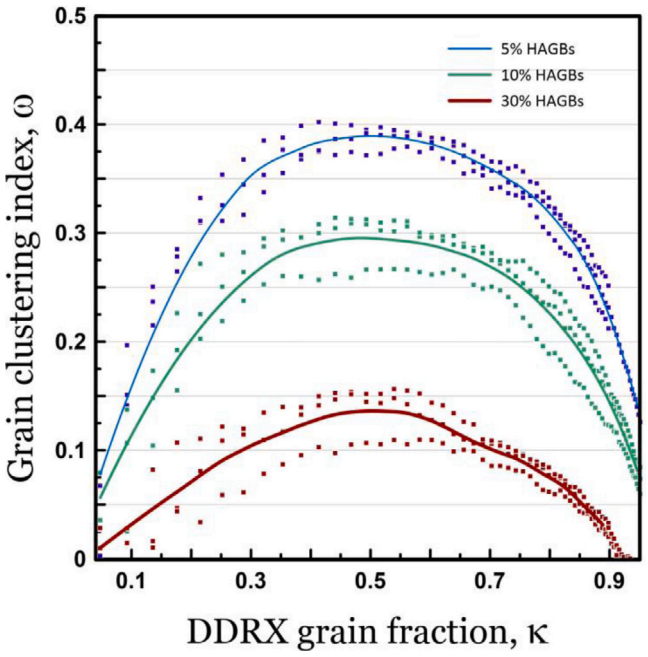

Fig. 4. Dependence of the clustering index ω on the grain fraction κ for different initial HAGBs fractions: $p_0 = 0.05$, $p_0 = 0.1$, and $p_0 = 0.3$. Results depicted by dots are obtained by the 2D model with three different randomly generated initial structures. Curves represent the least squares interpolations between dots.

2.2.2. *Three-dimensional structure evolution during DDRX*

Fig. 5 shows an example of the 3000-grain Voronoi tessellation of an elongated 3-dimensional cuboid which was used for DDRX studies. For these simulations, an initial state with a small amount of 5% ($p_0 = 0.05$) randomly distributed HAGBs has been used.

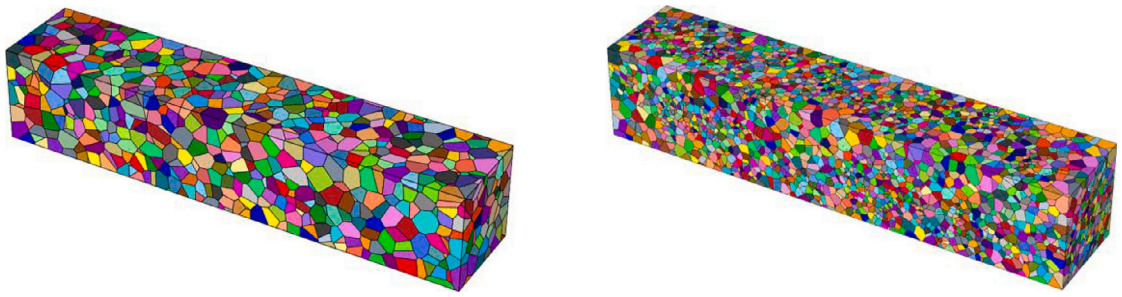

(a) (b)

Fig. 5. Simulation of DDRX on a 3D structure: (a) initial structure of 3000 polyhedrons with $\kappa = 0$; and (b) final structure of 58,617 polyhedrons with $\kappa = 0.95$.

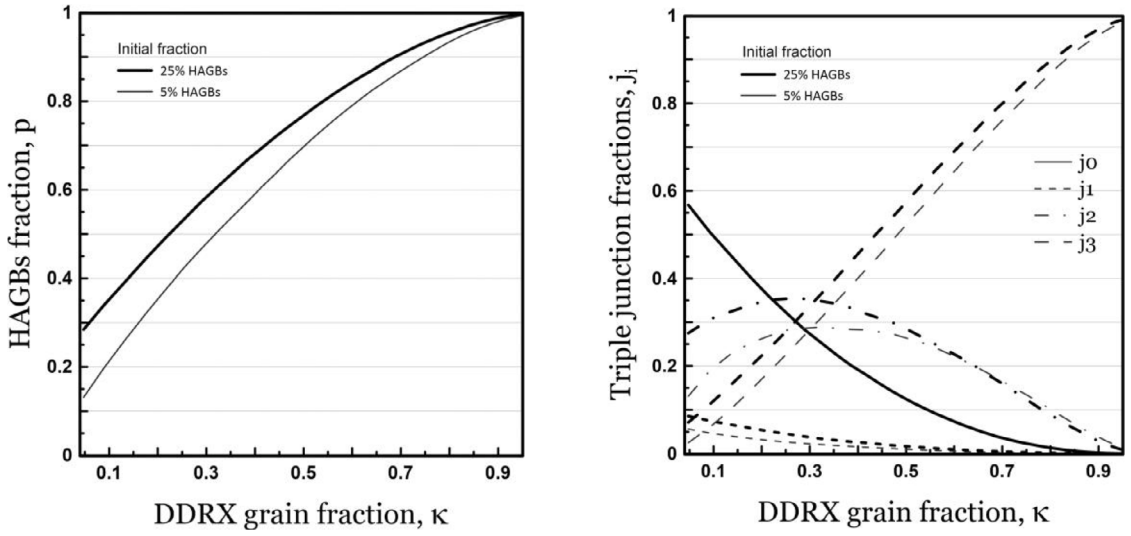

(a) (b)

Fig. 6. Evolution of the (a) HAGBs fraction p and (b) TJ fractions j_i during DDRX in 3D structures with the initial HAGBs fractions $p_0 = 0.05$ and $p_0 = 0.25$.

The two pictures show grain structures of the initial state represented by the 3000-grain Votonoi tessellation (Fig. 5(a)) and 58,617-grain tessellation obtained as a result of the DDRX process. Both grain refining and a considerable level of inhomogeneity, leading to a bimodal distribution of grain sizes, can be clearly seen.

The fraction of HAGBs p, as expected, grows monotonically (Fig. 6(a)) with the number of DDRX grains κ. The difference between DDRX and CDRX [42,44] is in the evolution of the fractions of TJs of different types j_i [43]. Fig. 6(b) shows the evolution of all TJ types at two different initial fraction of HAGBs $p_0 = 0.05$ and $p_0 = 0.25$. Both distributions are drastically different from the ones observed as the result of CDRX [42,44]. While the j_2 fraction remains similar in both cases, the j_1 fraction is extremely small, and, correspondingly, the j_3 fraction becomes very large in the DDRX process contrasting to the TJ types distribution observed after CDRX [42,44]. Therefore, the j_3 fraction can be suggested as a reliable indicator of the DDRX mechanism, especially at small and moderate fractions of recrystallised grains κ.

The range of $\omega \in [0, 0.25]$ observed in Fig. 7(a) indicates a moderate degree of clustering in the spatial distribution of DDRX grains. This can also be seen in the 2D example of structure evolution during DDRX presented in Fig. 3: a whole DDRX process develops around a few centres of recrystallisation with a high density of DRX grains (and so small average grain size), which increases with distance gradually. The specific "pattern" of new grains strongly depends on the initial spatial distribution of HAGBs and the local grain geometry.

The configuration entropy is a cumulative characteristic showing the diversity in all the four TJ types. Its large values indicate high diversity with a nearly equal probability of TJs of any type. The maximum value of the configuration entropy is always attained at a fraction of HAGBs equal to $p = 0.5$ independently of the particular process of structure evolution. Oppositely, the fraction of DDRX grains κ corresponding to this S_J maximum is the process-dependent characteristic, and, according to Fig. 7(b), the maximum of the configuration entropy is attained at $\kappa \approx 0.35$ for the initial fraction of HAGBs $p_0 = 0.05$. The observed maximum value of the entropy in the 2D case is about $S_J \approx 1.7$.

Another essential point which needs to be addressed is the possible existence of considerable initial HAGB microstructure that appeared as the result of a preliminary CDRX recrystallisation process before the initiation of the DDRX process. Consider initial plastic strain after CDRX $\varepsilon_{pl} \approx 1$, which is achievable inside adiabatic shear bands in the considered aluminium alloys. The initial HAGBs microstructure with $p_0 = 0.25$ and the TJ types distribution close to the one experimentally observed after CDRX has been created by the grain rotation simulation procedure described in [42] by means of the open-sourced PCC Processing Design code [57].

Fig. 6 shows the slightly higher values of p and j_1, j_2 and j_3 compared to the previous case of $p_0 = 0.05$, indicating a broader spatial spread (much smaller fraction j_0) of HAGBs. At the same time, configuration entropy can be larger or smaller depending on the DDRX grain fraction κ (Fig. 7(b)), but it remains larger than in the case of the random spatial distribution of HAGBs [44] demonstrating higher

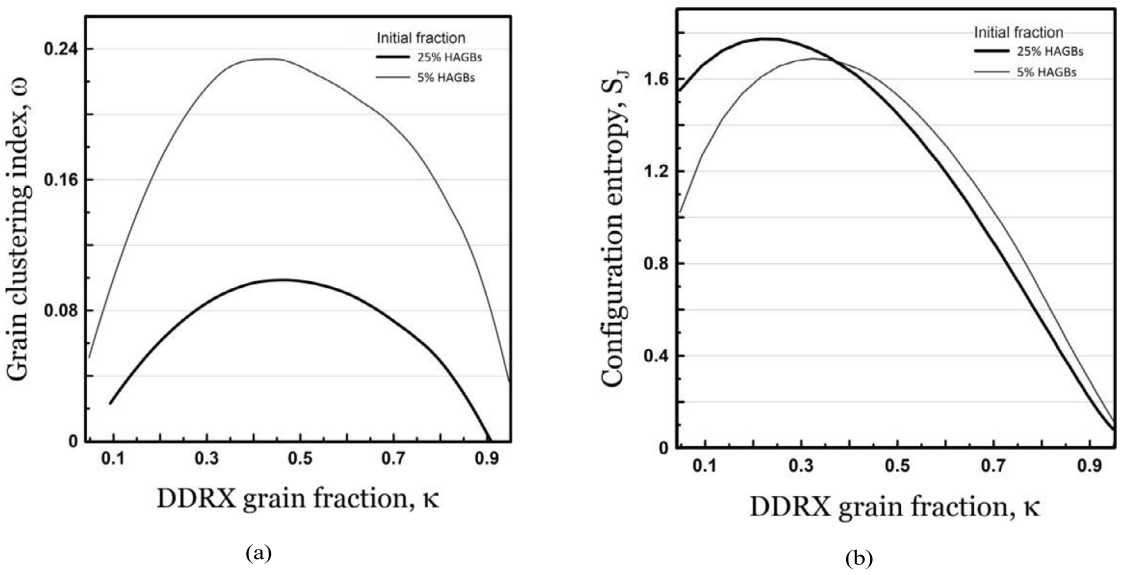

Fig. 7. Evolution of the (a) clustering index ω, and (b) TJ configuration entropy S_J during DDRX simulations of 3D structures with the initial HAGBs fractions $p_0 = 0.05$ and $p_0 = 0.25$.

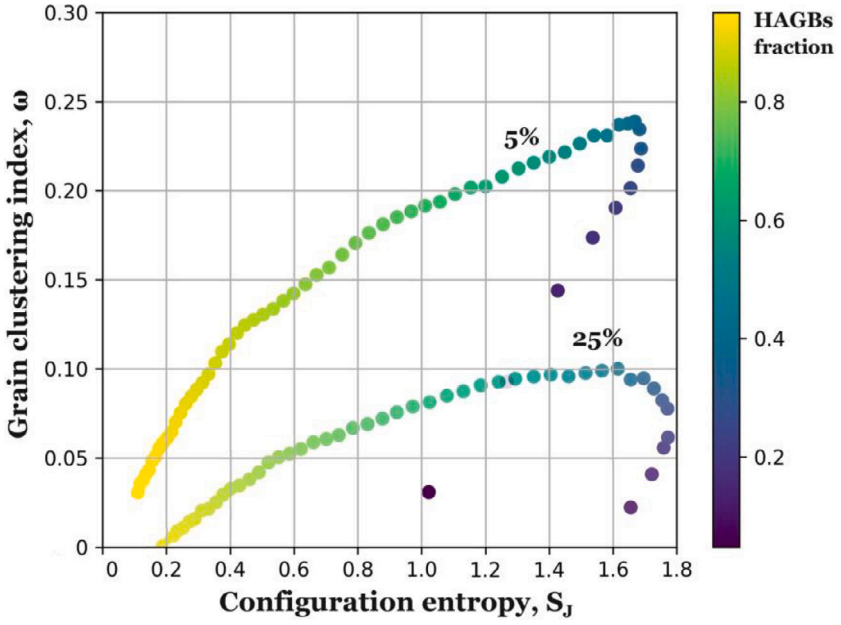

Fig. 8. Relation between the DDRX grain clustering index ω and the TJ configuration entropy S_J during DDRX in 3D structures with the initial fractions of HAGBs $p_0 = 0.05$ and $p_0 = 0.25$.

diversity of the TJ types. The clustering index $\omega \in [0, 0.1]$ shown in Fig. 7(a) became more than twice smaller at $p_0 = 0.25$ compared to the case of $p_0 = 0.05$ indicating much larger homogeneity in the spatial distribution of DDRX grains.

Fig. 8 shows the ratio between the ω and the configuration entropy S_J for structure evolution in the two considered cases: 5% of the initial fraction of HAGBs and 25% of the initial fraction of HAGBs. The clustering index follows the same trend (is proportional to) as the configuration entropy before and after the S_J maximum. It suggests that more intense clustering of grains leads to a larger diversity in the TJ types during DDRX.

In particular, it opens a simple method of estimation ω based on the measurements of S_J values using EBSD maps. The latter is much easier to implement as only TJ fractions j_i are needed, while the reconstruction of the DDRX grains for calculation ω is a much more complicated task.

2.3. Physical model of grain nucleation and growth during DDRX

The developed purely combinatorial model cannot predict the microstructure development in time as it contains only structural characteristics. A mapping of structural characteristics such as j_i, ω and S_J should be provided by an appropriate kinetic model for the nucleation rate of new DDRX grains $\kappa(t)$. There are several physical kinetic models for the nucleation of DRX grains and the evolution of related parameters, such as average grain size of material [24,32–36]. Let us consider

the model [33] with a simple kinetic function for the grain nucleation rate per unit area in the form:

$$\dot{n} = k \cdot \left(\rho_D\right)^q, \tag{10}$$

where ρ_D is an average scalar dislocation density [30,63] (a total length of dislocation lines per unit volume), q is a model parameter calculated in [33] as $q = 3$, and k is a parameter dependent on temperature and strain-rate sensitivity. The dependence is expressed by the Arrhenius law [33]:

$$k = k_0 \cdot \dot{\varepsilon}_{pl} \exp\left(-\frac{Q_n}{RT}\right), \tag{11}$$

where Q_n is the activation energy for nucleation of a new grain, which for aluminium alloys varies weakly and can be estimated as $Q = 180$ kJ/mol [64,65], $R = 8.31$ J/mol K is the gas constant, T is the temperature in Kelvin, $\dot{\varepsilon}_{pl}$ is the plastic strain rate, and k_0 is a high-temperature limit which, according to the data provided in [33], can be estimated as $k_0 \approx 7 \cdot 10^{-24}$ m^4/s.

An average dislocation density ρ_D in the dynamically loaded aluminium alloys can be estimated using the dislocation kinetic models [13,63,66,67]. To simplify the calculations, we use an average value $\rho_D = 10^{14}$ m^{-2} typical for metals subjected to shock-wave loading with medium strain rates of about $\dot{\varepsilon}_{pl} = 10^4$ s^{-1}. Such strain rates are usual for split Hopkinson bars impact tests and have been achieved in the FEM simulations reported in this work.

Finally, the number of newly created DDRX grains as a function of time is calculated by integrating Eq. (10) with respect to time, taking into account the whole temperature history including heating and cooling stages:

$$n(t) = k_0 \cdot \dot{\varepsilon}_{pl} \cdot \rho_D^q \int_{t_0}^{t} \exp\left(-\frac{Q_n}{RT(s)}\right) ds, \tag{12}$$

In this equation, s is the time variable changing in the range from t_0 to a maximum integration limit t_∞. The temperature must be close to its ambient value $T_a \approx 300$ K at both time limits. For obtaining the realistic temperature history $T(t)$ inside the adiabatic shear bands, macroscopic numerical FEM simulations are performed as described in the following section.

3. FEM simulations of high-strain-rate impact loading of AA1050 and AW5083 aluminium alloys

3.1. Material's heating and cooling inside adiabatic shear bands

Consider a DDRX process inside adiabatic shear bands in two aluminium alloys — AA1050 and AW5083. The first series 1050 is the aluminium of technical purity — very useful for comparison with other alloys, while the 5083 alloys are widely used in the automotive and marine industries due to their good weldability and excellent corrosion resistance [50].

The spatial distribution of the temperature and the cooling rate are material- and process-dependent. Precise temperature measurements during high-strain-rate impact loading is a challenging task. Here, this distribution is calculated with an appropriately fitted and tested FEM model. The numerical approach adopted is widely used for simulation of experiments for which the developed DDRX model is applicable: a high-strain-rate impact loading of hat-shaped samples [5,8,49] in a Split Hopkinson Pressure Bars (SHPB) [8,68,69]. The LS-Dyna commercial software [51,70] is specifically designed for simulation of high-rate impact processes. It incorporates all mechanical and physical models suitable for simulations of high-strain-rate plasticity. Furthermore, it allows to output of the temperature history at each finite element for further use this data as input to the discrete DDRX model.

Table 1
Parameters of the Johnson–Cook constitutive equation with the fracture kinetic model, and Mie–Gruneisen equation of state for the considered AA1050 and AW5083 aluminium alloys.

J-C:	σ_y, MPa	B, MPa	C	n	m	T_m, K
AA1050 [71]	140	350	0.001	0.183	0.859	923
AW5083 [72]	167	596	0.001	0.55	0.859	893
Fracture:	σ_c, GPa	D_1	D_2	D_3	D_4	D_5
AA1050 [71]	−1.5	0.071	1.248	−1.142	0.0097	0.0
AW5083 [72]	−1.5	0.0261	0.263	−0.349	0.147	16.8
Gruneisen:	c_l, m/s	s	γ	a		
AA1050 [73]	5328	1.4	1.97	0.48		
AW5083 [73]	5240	1.4	1.97	0.48		

3.1.1. Johnson-Cook and Mie–Gruneisen models with parameters fitted for 1000 and 5000 series aluminium alloys

Several mechanical and physical properties of aluminium alloys can be taken as common for all alloy types: material density (2700 kg/m^3), shear modulus ($G = 27$ GPa), Young modulus ($E = 72$ GPa), Poisson's ratio ($\nu = 0.3$), and specific heat capacity ($c = 920$ J kg^{-1} K^{-1}) [71,72]. Other properties depend on the alloy series but are common for alloys of the same series.

Three empirical models are used to describe the plasticity, fracture and thermodynamic state of the considered alloy series. The classical Johnson–Cook constitutive equation with the kinematic fracture empirical model [71,72] is incorporated in LS-Dyna [51] and most of the other commercial FEM packages. While the accuracy of these models in a wide range of high-strain-rate deformation processes has not been demonstrated, they provide realistic values of the dynamic yield strength σ_y^d and the critical plastic strain ε_{pl} for fracture initiation at moderate strain rates in the range $10^3 - 10^4$ s^{-1} typical for the considered SHPB tests. The set of the empirical parameters fitting the mechanical behaviour of AA1050 and AW5083 alloys has been taken from the works [71,72], and is shown in Table 1. The relation between the pressure P and the temperature T, is given by the Mie–Gruneisen equation [73]:

$$P = \begin{cases} \frac{\rho_0 c_l^2 \mu \left(1+(1-0.5\Gamma)\mu-0.5\Gamma\mu^2\right)}{(1-(s-1)\mu)} + (1+\mu)\Gamma \cdot E, \mu > 0 \\ \rho_0 c_l^2 \mu + (1+\mu)\Gamma \cdot E, \mu < 0. \end{cases} \tag{13}$$

where $\Gamma = (\gamma + a\mu)/(1+\mu)$, γ is the Gruneisen parameter, relative material density $\mu = \rho/\rho_0 - 1$, ρ_0 and ρ are the initial and the current material densities, respectively; E is the internal energy per initial specific volume, and c_l is a parameter with values close to the longitudinal sound velocity. This equation of state is simultaneously simple and works well at high-strain-rate deformation conditions in the absence of phase transitions. The four parameters (c_l, s, γ and a) are taken from [73] and are also shown in Table 1.

While their thermodynamic parameters differ slightly, there are large differences in the deformation and fracture behaviour of the aluminium of technical purity 1000 series and the 5000 series of aluminium alloys.

Material heating due to plastic deformation is determined by the efficiency of the thermo-mechanical conversion, expressed by the Taylor–Quinney Coefficient (TQC) or the Inelastic Heat Fraction (IHF). In this work the value of TQC is taken to be equal to $Q = 0.9$, following the conventional approach for metals [74]. It should be noted that in the case of high-strain-rate deformation, some authors report values of TQC different from 0.9 (see ex. [75]). The ambient temperature has been taken as $T_a = 300$ K.

3.2. FEM model and its LS-Dyna implementation

Conditions corresponding to SHPB experiments (see e.g., [68]) were simulated with LS-Dyna commercial software [70]. LS-Dyna and other

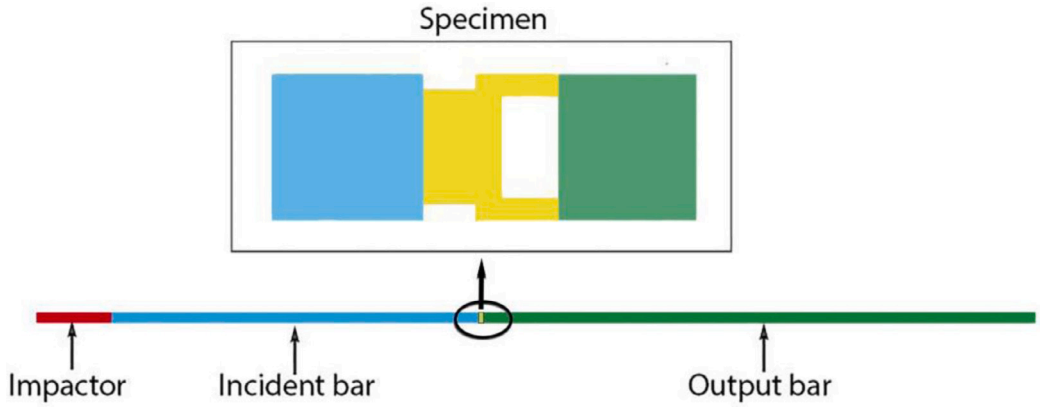

Fig. 9. Split Hopkinson Pressure Bars experimental geometry corresponding to the FEM model used for LS Dyna simulations.

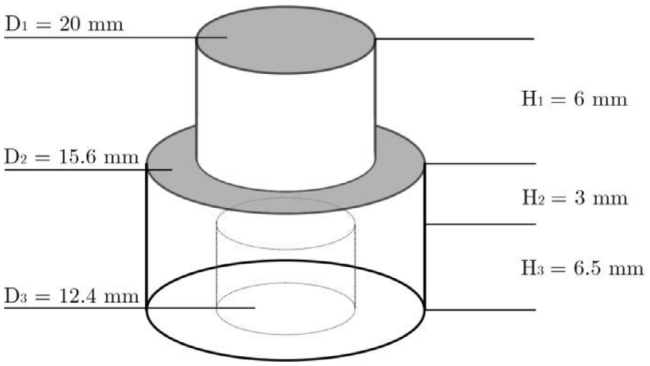

Fig. 10. Hat-shaped specimen geometry used for simulations.

FEA software have been used by various authors to simulate SHPB experiments demonstrating remarkable agreement with experimental observations (see e.g., [76]). The geometry of the experimental setup and the specimen is given in Fig. 9.

The impactor, the incident bar, and the output bar are made of Silver Steel (Young's modulus Y_s = 207 MPa, Poisson's Ratio ν_s = 0.3, density ρ_s = 7830 kg/m^3) and are simulated as linear elastic material. All of them are rods with diameters 0.02 m and lengths 0.2 m, 1.0 m, and 1.5 m, respectively. Hat-shaped specimen geometry [9] is used for both considered alloys, see Fig. 10.

In the SHPB experiments, the impactor is accelerated to a preset velocity by a gas gun. It collides with the input bar, creating a compression wave travelling along the bar. The compression wave passes through the specimen causing its deformation. During this deformation, the incident wave is partly transmitted into the output bar and partly reflected back into the incident bar. The incident, transmitted, and reflected waves can be measured using strain gauges attached to the incident and the output bars. The measurements provide information for analysis of sample deformation based on the Kolsky method [77].

Taking into account the axial symmetry of the entire problem, the FEM model was developed using 2D axisymmetric elements available in LS-Dyna. The developed model was tested for convergence and compared to available experimental measurements to guarantee the accuracy of the numerical scheme. For each of the sample geometries threshold impactor velocity (maximum impactor velocity not leading to sample fracture) was evaluated. Fig. 11 shows typical specimen geometry for (a) under-threshold and (b) over-threshold impactor velocities. As expected, for the studied experimental conditions and specimen geometry, deformation is localised in a narrow region, causing the appearance of an adiabatic shear band (see an ASB on Fig. 11(a)). For over-threshold impactor velocities, this localised deformation is causing intensive heat generation, inducing changes to material behaviour (following the Gruneisen EOS) and fracture, as predicted by the used kinematic fracture J-C model [71,72] (see Fig. 11(b)).

The DDRX model requires full temperature history within ASB formed in the deformed sample. The temperature history for all finite elements in the FEM model was recorded for the further analysis of grain structure evolution in the case of threshold impactor velocity. Fig. 12 shows a typical distribution of temperature within a specimen made of AW5083 aluminium alloy.

It can be seen that considerable heating, exceeding the initial temperature by more than 100 degrees, is observed only locally within the narrow region of ASB.

4. DDRX inside adiabatic shear bands

Joining together structural model for DDRX evolution with the FEM-based temperature function for new grain nucleation $\dot{n}(t)$ (Eq. (12)) allow to study the number of DRX grains, and the grain clustering index $\omega(t)$ as functions of processing time t. The nucleation of new DDRX grains depends on the temperature history (see Eq. (12)), which in turn, is a function of the plastic deformation process as described in Section 2.3. To calculate the number of newly formed DDRX grains as a function of time $n(t)$ inside ASB, Eq. (12) was integrated for both studied alloys. This allows for calculating $\kappa(t)$ and re-plotting Figs. 7(a) or 7(b) as functions of time. The key point is that the simulation results of microstructure evolution, such as those shown in Figs. 7(a) and 7(b), can be reused for calculating grain microstructures at different spatial points (finite elements) at different moments of time, according to their local temperature histories.

The initial pressure wave, initiated by the impactor, reflects from the free surfaces of the sample and Hopkinson rods. As a result, several stress waves propagate throughout the sample, causing from one to three temperature peaks. In turn, the temperature peaks lead to peaks in new grains as seen in Figs. 13(a) and 14(a). The microsecond-long time frame is appeared to be large enough for DDRX nucleation of new grains at these temperatures in the considered aluminium alloys. It is interesting to note, that the first peak in Fig. 13(a), occurring around 40 degrees Celsius, appears to be insufficient for driving DDRX and such temperature increase does not lead to nucleation of a notable number of new recrystallised grains.

It should be also noted that the exponent in Eq. (12) causes a criticality which can be seen as abrupt growth of ω in Figs. 13(b) and 14(b). The maximum clustering is achieved after the temperature peak during the cooling stage because some "incubation" time $\tau_{inc} \approx 0.1$ μs is required for the full development of DDRX.

The temperature increase ΔT obtained by FEM simulations at different spatial points of the sample is presented in Fig. 15(a),(b). Both

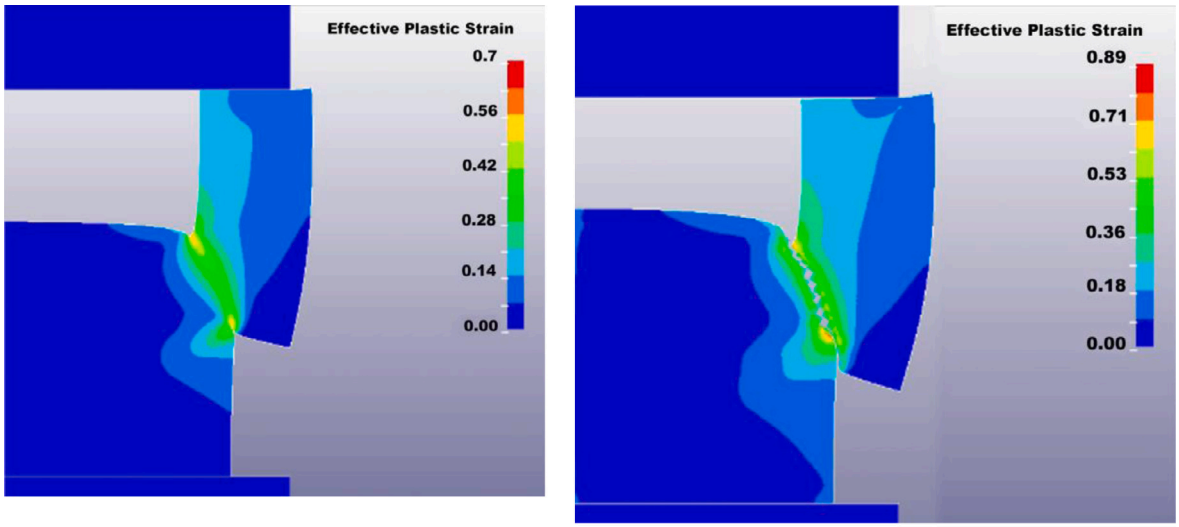

Fig. 11. Specimen geometry for (a) under-threshold and (b) over-threshold impactor velocities. The contour plot shows the distribution of effective plastic strain within the deformed sample made of AW5083 aluminium alloy.

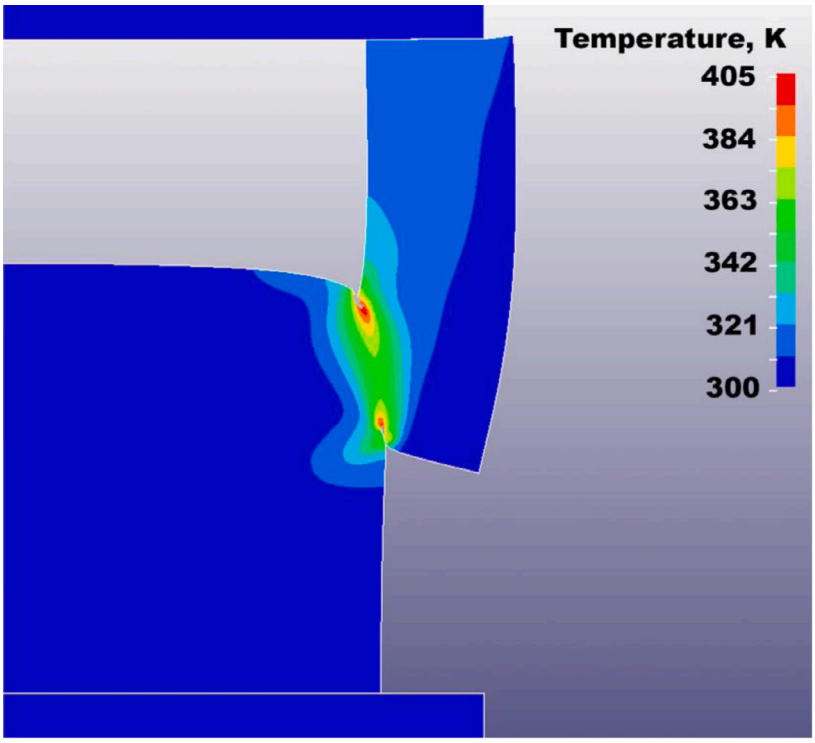

Fig. 12. Typical distribution of temperature within a specimen made of AW5083 aluminium alloys.

figures correspond to the time instances close to the maximum temperature achieved in the samples (see Figs. 13 and 14), where the most significant structural changes happened. Because of the axial symmetry of the hat-shaped specimens, only the 2D section and the corresponding 2D distribution of structural characteristics across ASB can be shown.

Because of the adiabatic deformation conditions, the temperature in the considered alloys can rise up to hundreds of degrees several times during a few microseconds-long deformation process caused by the propagation of a stress wave. At maximum, they demonstrate a rather homogeneous spatial distribution of temperatures inside the ASBs with a large temperature gradient across the bands.

The mapping of the structural data presented in Figs. 7(a) and 7(b) using Eq. (12) and the temperature histories shown in Figs. 13(a) and 14(a) at different spatial points at the time close to the end of the cooling stage ($t \approx 3$ ms) provides the final spatial distributions of ω and S_J in the samples. These are shown in Figs. 16 and 17, respectively. While the temperature at its maximum is almost homogeneously distributed inside shear bands, the spatial distribution of ω and S_J is strongly heterogeneous (Fig. 15).

The "critical" nature of the DDRX kinetics due to its exponential dependence on temperature, and the spatial strain inhomogeneities along ASB, leads to strong spatial gradients in structural characteristics inside the areas affected by DDRX — much greater compared to the corresponding temperature gradient. The affected areas are concentrated around the edges of the considered hat-shaped samples, leaving the

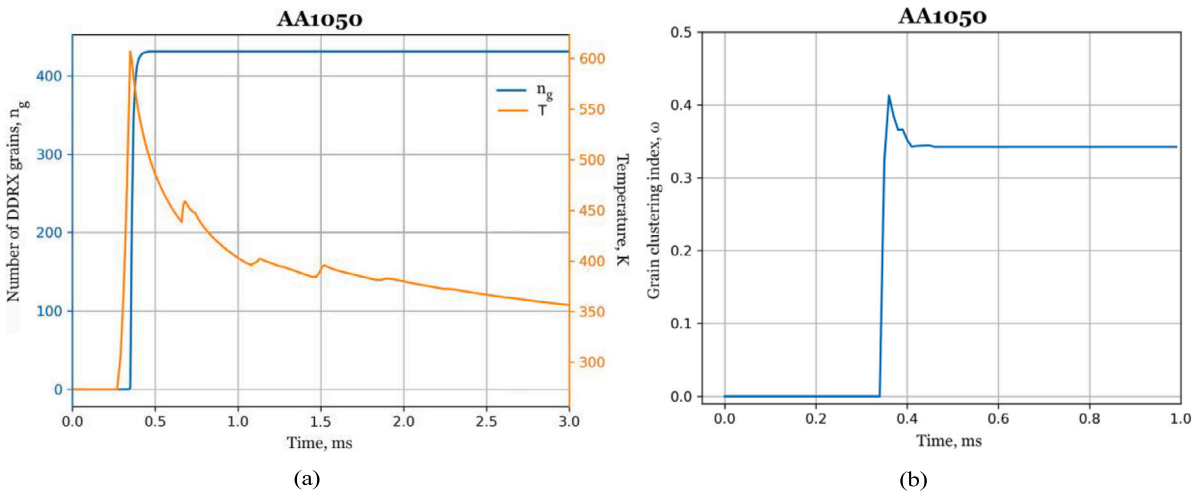

Fig. 13. DDRX in ASB of AA1050 alloy: (a) Temperature history $T(t)$ and the corresponding number of DDRX grains $n_g(t)$; (b) DDRX grain clustering index $\omega(t)$.

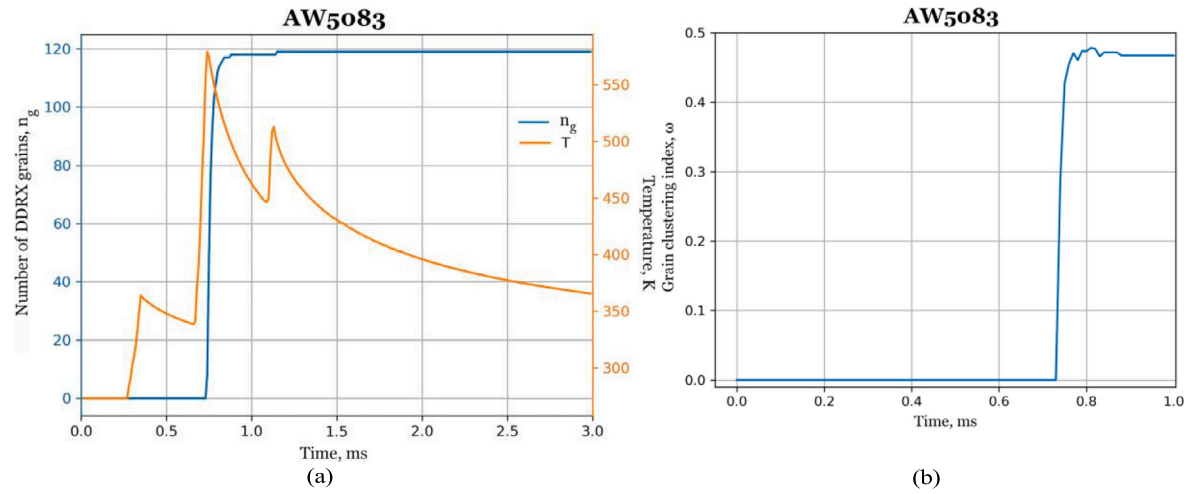

Fig. 14. DDRX in ASB of AW5083 alloy: (a) Temperature history $T(t)$ and the corresponding number of DDRX grains $n_g(t)$; (b) DDRX grain clustering index $\omega(t)$.

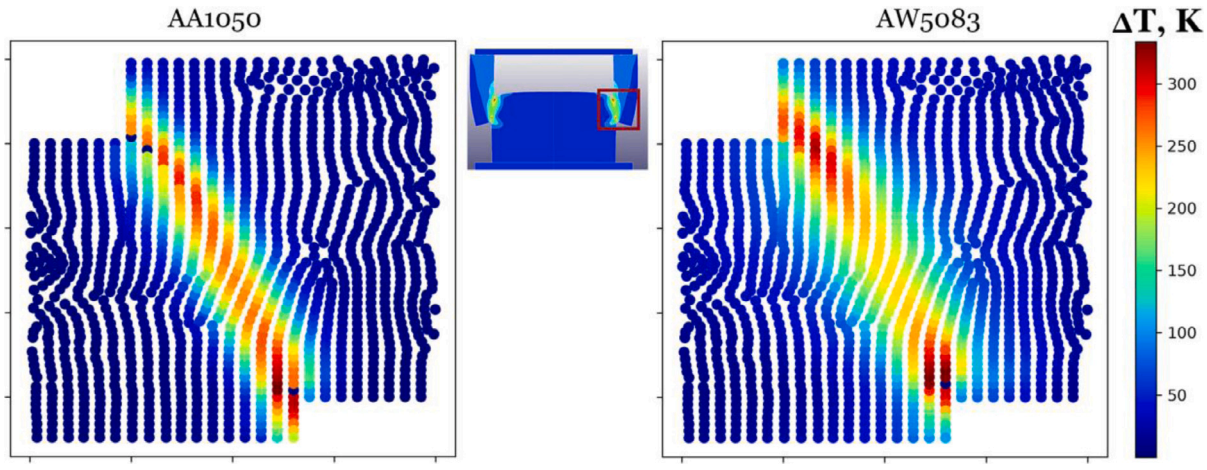

Fig. 15. FEM simulations of the spatial distribution of temperature increase ΔT in a diametral 2D cut in (left) AA1050 at the time 350 ns and (right) AW5083 at the time 740 ns.

central part of the shear bands mostly untouched. This is very different from the cases of severe plastic deformation at quasi-static deformation conditions, such as ECAP or cold-rolling processing of aluminium and copper alloys [16,18]. In the quasi-static case, there is enough time for the material for cooling during the deformation process, and CDRX is often the only mechanism contributing to microstructural changes [14].

Notably, in the dynamic case, it is much more difficult than in the quasi-static SPD processes to separate the temperature-governed

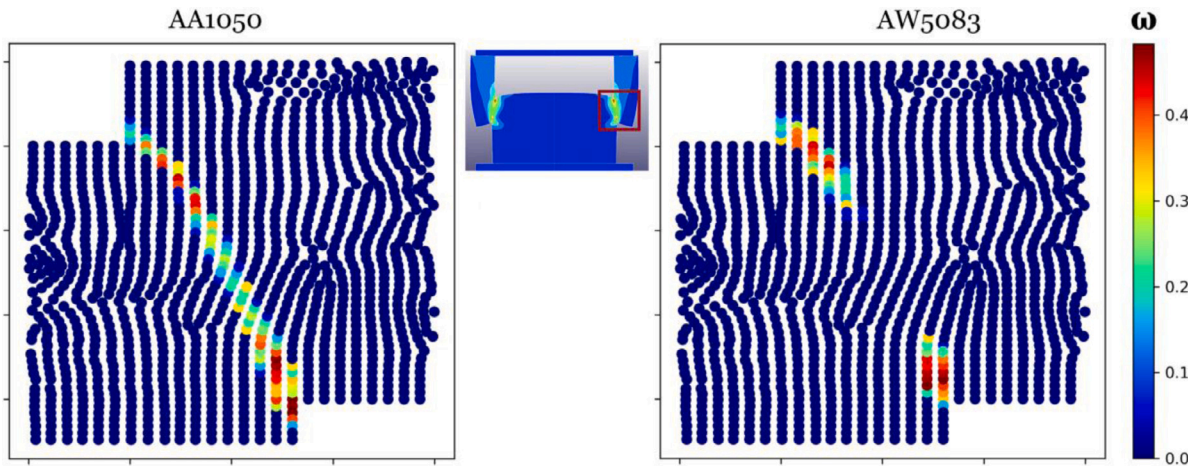

Fig. 16. Spatial distribution of the clustering index ω in (left) AA1050 and (right) AW5083 alloys at the end of the cooling stage ($t = 3$ μs).

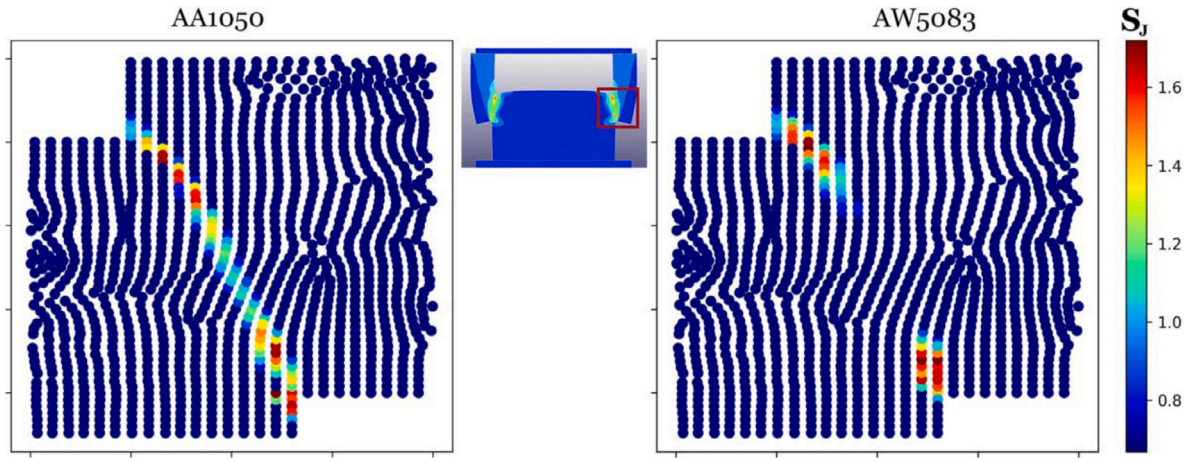

Fig. 17. Spatial distribution of the TJ configuration entropy S_J in (left) AA1050 and (right) AW5083 alloys at the end of the cooling stage ($t = 3$ μs).

nucleation-and-growth DDRX process from the CDRX caused by grain rotations [42]. Even in geometrically simple and symmetric areas such as ASB, the evolution of DDRX microstructure appeared to be very complex, creating large spatial gradients of structural characteristics both along and across ASB. Such complexity makes it difficult to draw general conclusions about the structure evolution inside ASB and requires further comprehensive studies. One key aspect is the interrelation between the CDRX and DDRX mechanisms of recrystallisation. The performed simulations demonstrate that the alloy type, the impactor velocity, and the sample geometry can cause drastically different DDRX microstructures with large variations along the bands.

5. Discussion and conclusions

The ability to predict and model dynamic recrystallisation is critical for managing plastic flow instabilities and workability of alloys during the industrial forming based on the severe plastic deformation with elevated temperatures [1]. The Zenner–Hollomon parameter Z was employed by many researchers [5,22,37,78] as an effective engineering indicator of the material's propensity to localisation [22]. It is inversely proportional to the expression for the DDRX grain nucleation rate commonly used in recrystallisation models [31,37], and so in many cases, it correlates well with the evolution of an average grain size of a material [21,31]. It is assumed that the large values of $lnZ > 25$ indicate the high level of the DDRX grain clustering and larger accumulation of deformation energy in the defect microstructure. Unfortunately, all these outcomes were verified only for a few metals and quasistatic deformation conditions $\dot{\varepsilon} \sim 10^{-3} - 1\ s^{-1}$ with very few qualitative results for high-strain-rate deformation conditions $\dot{\varepsilon} \sim 10^{2} - 10^{6}\ s^{-1}$. The only general assumption that was made was about the similarities of structures obtained at the similar values of Zenner–Hollomon parameter [5].

The present study questions the universal applicability of the Zenner–Hollomon parameter as the reliable descriptor allowing to predict the final materials microstructure after the deformation processing. The results of our simulations demonstrate high sensitivity of the meso-structural characteristics to microscopic features such as the local arrangements of HAGBs expressed by the value of TJ configuration entropy S_J. Similar effects of promoting DDRX locally by producing high local densities of dislocations and the new grain nucleation sites were reported earlier as the particle-stimulated nucleation (PSN) mechanism [22]. But in contrast with particles and local stress concentrators, the fraction and spatial distribution of HAGBs strongly depend on the preliminary CDRX process and the transition moment between CDRX and DDRX mechanisms. The homogeneous spatial distribution of local agglomeration of HAGBs, indicated by high values of S_J and j_3 TJ fraction, leads to a uni-modal distribution of grain sizes instead of the bi-modal typical for highly clustered structures and larger values of an average grain size inside ASBs. Preliminary cold severe plastic deformation can have a similar effect increasing the fraction of HAGBs by CDRX [42,44]. To convey such a complexity the DRX sensitivity rate has been recently introduced [22] and demonstrate a very large variation of Z in the range of lnZ from 24 to 28 at strain rates $\dot{\varepsilon} \sim 10^{-3} - 1\ s^{-1}$. Such sensitivity reveals, that the DDRX process can

be 'non-equilibrium' even at low strain rates. Our simulations reveal that at high strain rates, even relatively low temperature differences of about 100K can cause a significant gradient in the DDRX clustering in aluminium alloys promoting localisation.

The proposed discrete model can be seen as a following step in the research program of developing nucleation and growth models initiated in the works [20,31,40], where Monte-Carlo simulation technique was employed and the microstructure with its crystallographic orientations of each lattice element and its neighbours has been mapped onto a discrete, two-dimensional lattice with the use of the Potts model [31]. Later works [21,37,38] were based on the same principles but widely employed cellular automaton method to overcome limitations of Monte-Carlo simulations and make the DDRX dynamic more realistic, but all of them employed only relatively small 2-dimension lattices, naturally overlooked most of the topological complexity of a real material. In the present study, several previously proposed ideas were combined into a novel computation framework introducing a more realistic large-scale 3-dimension discrete model, combining the effect of grain structure topology with the realistic dynamic function for grain nucleation and the particular temperature history inside ASBs. It allowed for simulating for the first time the evolution of structural characteristics of aluminium alloys 1000 and 5000 series. The cell complexes [42,52] used for the DDRX simulations contained from 3000 to 70,000 grains, providing a statistically representative description of the recrystallisation process. In contrast to the continuous DDRX models, the proposed approach provides the opportunity to use structural characteristics of a new recrystallised grain structure such as configuration entropy [43,44] and grain clustering index [56]. It reveals the transition of microscopic local grain boundary arrangements into the mesoscale inhomogeneities in material microstructure and mechanical properties mediated by the grain nucleation process.

Further progress in this field requires more sophisticated simulations mixed CDRX and DDRX mechanisms of grain and grain boundary structure evolution alongside the acquisition of relevant experimental data that is the subject of our ongoing studies. Ultimately it should allow the creation of more advanced physically informed design of materials processing, taking into account (i) the initial distribution of HAGBs, twin boundaries, and particles; (ii) the effect of the preliminary CDRX process on the DDRX clustering and energy accumulation rate; and (iii) contribution from the spatial gradients of temperature and fraction of HAGBs to the grain structure evolution.

Declaration of competing interest

The authors declare that they have no known competing financial interests or personal relationships that could have appeared to influence the work reported in this paper.

Acknowledgements

Authors acknowledge the financial support from EPSRC, UK via grants EP/V022687/1 (PRISB) and EP/N026136/1 (GEMS). The authors confirm that the data supporting the findings of this study is available within the article. Some of the raw processed data required to reproduce these findings can be found on the http://materia.team project webpage.

References

[1] Chai L, Chai L, Huang W, Ma Y, Zhang Z. EBSD analysis on restoration mechanism of as-extruded AA2099 Al-Li alloy after various thermomechanical processes. Mater Chem Phys 2017;191:99–105. http://dx.doi.org/10.1016/j.matchemphys.2017.01.044.

[2] Prasad YVRK, Seshacharyulu T. Modelling of hot deformation for microstructural control. Int Mater Rev 1998;43:243–58. http://dx.doi.org/10.1179/imr.1998.43.6.243.

[3] Grass H, Krempaszky C, Werner E. 3-D FEM-simulation of hot forming processes for the production of a connecting rod. Comput Mater Sci 2006;36:480–9. http://dx.doi.org/10.1016/j.commatsci.2005.06.003.

[4] Lin CN, Tzeng YC, Lee SL, Fuh YK, Łukaszek-Sołek A, Lin CY, Chen MC, Pan TA. Optimization of hot deformation processing parameters for as-extruded 7005 alloys through the integration of 3D processing maps and FEM numerical simulation. J Alloys Compd 2023;948. http://dx.doi.org/10.1016/j.jallcom.2023.169804.

[5] Xu Y, Zhang J, Bai Y, Meyers MA. Shear localization in dynamic deformation: Microstructural evolution. Metall Mater Trans A 2008;39 A:811–43. http://dx.doi.org/10.1007/s11661-007-9431-z.

[6] Walley SM. Shear localization: A historical overview. Metall Mater Trans A 2007;38 A:2629–54. http://dx.doi.org/10.1007/s11661-007-9271-x.

[7] Bai YL, Bai J, Li HL, Ke FJ, Xia MF. Damage evolution, localization and failure of solids subjected to impact loading. Int J Impact Eng 2000;24:685–701. http://dx.doi.org/10.1016/S0734-743X(99)00151-7.

[8] Zhang W, He L, Lu Z, Kennedy GB, Thadhani NN, Li P. Microstructural characteristics and formation mechanism of adiabatic shear bands in Al–Zn–Mg–Cu alloy under dynamic shear loading. Mater Sci Eng A 2020;791:139430. http://dx.doi.org/10.1016/j.msea.2020.139430.

[9] Yan N, Li Z, Xu Y, Meyers MA. Shear localization in metallic materials at high strain rates. Prog Mater Sci 2021;119:100755. http://dx.doi.org/10.1016/j.pmatsci.2020.100755.

[10] Dodd B, Bai Y, editors. Adiabatic shear localization (second edition). 2nd ed.. Oxford: Elsevier; 2012, p. 468. http://dx.doi.org/10.1016/B978-0-08-097781-2.00011-3.

[11] Wright TW, editor. The physics and mathematics of adiabatic shear bands. Cambridge monographs on mechanics, Cambridge University Press; 2002, p. 260, URL: https://www.cambridge.org/us/universitypress/subjects/mathematics/fluid-dynamics-and-solid-mechanics/physics-and-mathematics-adiabatic-shear-bands?.

[12] Meyers MA, Nesterenko VF, Lasalvia JC, Xue Q. Shear localization in dynamic deformation of materials: microstructural evolution and self-organization. Mater Sci Eng 2001;317:204–25. http://dx.doi.org/10.1016/S0921-5093(01)01160-1.

[13] Mayer AE, Borodin EN, Mayer PN. Localization of plastic flow at high-rate simple shear. Int J Plast 2013;51:188–99. http://dx.doi.org/10.1016/j.ijplas.2013.05.005.

[14] Sakai T, Belyakov A, Kaibyshev R, Miura H, Jonas JJ. Dynamic and post-dynamic recrystallization under hot, cold and severe plastic deformation conditions. Prog Mater Sci 2014;60(1):130–207. http://dx.doi.org/10.1016/j.pmatsci.2013.09.002.

[15] Huang K, Logé RE. A review of dynamic recrystallization phenomena in metallic materials. Mater Des 2016;111:548–74. http://dx.doi.org/10.1016/j.matdes.2016.09.012.

[16] Morozova A, Borodin E, Bratov V, Zherebtsov S, Belyakov A, Kaibyshev R. Grain refinement kinetics in a low alloyed Cu-Cr-Zr alloy subjected to large strain deformation. Materials (Basel) 2017;10(12):1394. http://dx.doi.org/10.3390/ma10121394.

[17] Borodin E, Jivkov AP, Sheinerman AG, Gutkin MY. Optimisation of rGO-enriched nanoceramics by combinatorial analysis. Mater Des 2021;212:110191. http://dx.doi.org/10.1016/j.matdes.2021.110191.

[18] Bodyakova A, Tkachev M, Raab GI, Kaibyshev R, Belyakov AN. Regularities of microstructure evolution in a Cu-Cr-Zr alloy during severe plastic deformation. Materials (Basel) 2022;15(16):5745. http://dx.doi.org/10.3390/ma15165745.

[19] Xie B, Zhang B, Yu H, Yang H, Liu Q, Ning Y. Microstructure evolution and underlying mechanisms during the hot deformation of 718Plus superalloy. Mater Sci Eng A 2020;784:139334. http://dx.doi.org/10.1016/j.msea.2020.139334.

[20] Peczak P, Luton MJ. The effect of nucleation models on dynamic recrystallization: II. Heterogeneous stored-energy distribution. Phil Mag B 1994;70:817–49. http://dx.doi.org/10.1080/01418639408240254.

[21] Zhang C, Zhang L, Xu Q, Xia Y, Shen W. The kinetics and cellular automaton modeling of dynamic recrystallization behavior of a medium carbon Cr-Ni-Mo alloyed steel in hot working process. Mater Sci Eng A 2016;678:33–43. http://dx.doi.org/10.1016/j.msea.2016.09.056.

[22] Li L, Wang Y, Li H, Jiang W, Wang T, Zhang C-C, Wang F, Garmestani H. Effect of the Zener-Hollomon parameter on the dynamic recrystallization kinetics of Mg–Zn–Zr–Yb magnesium alloy. Comput Mater Sci 2019;166:221–9. http://dx.doi.org/10.1016/j.commatsci.2019.05.015.

[23] Yanagida A, Yanagimoto J. A novel approach to determine the kinetics for dynamic recrystallization by using the flow curve. J Mater Process Technol 2004;151(1):33–8. http://dx.doi.org/10.1016/j.jmatprotec.2004.04.007.

[24] Chen X-M, Lin Y, Wen D-X, Zhang J-L, He M. Dynamic recrystallization behavior of a typical nickel-based superalloy during hot deformation. Mater Des 2014;57:568–77. http://dx.doi.org/10.1016/j.matdes.2013.12.072.

[25] Estrin Y, Vinogradov A. Extreme grain refinement by severe plastic deformation: A wealth of challenging science. Acta Mater 2013;61(3):782–817. http://dx.doi.org/10.1016/j.actamat.2012.10.038.

[26] Raab GJ, Valiev RZ, Lowe TC, Zhu YT. Continuous processing of ultrafine grained Al by ECAP-Conform. Mater Sci Eng A 2004;382(1–2):30–4. http://dx.doi.org/10.1016/j.msea.2004.04.021.

[27] Valiev RZ, Langdon TG. Principles of equal-channel angular pressing as a processing tool for grain refinement. Prog Mater Sci 2006;51(7):881–981. http://dx.doi.org/10.1016/j.pmatsci.2006.02.003.

[28] Valiev RZ, Islamgaliev RK, Alexandrov IV. Bulk nanostructured materials from severe plastic deformation. Prog Mater Sci 2000;45(2):103–89. http://dx.doi.org/10.1016/S0079-6425(99)00007-9.

[29] Mishra A, Kad BK, Gregori F, Meyers MA. Microstructural evolution in copper subjected to severe plastic deformation: Experiments and analysis. Acta Mater 2007;55(1):13–28. http://dx.doi.org/10.1016/j.actamat.2006.07.008.

[30] Bratov V, Borodin EN. Comparison of dislocation density based approaches for prediction of defect structure evolution in aluminium and copper processed by ECAP. Mater Sci Eng A 2015;631:10–7. http://dx.doi.org/10.1016/j.msea.2015.02.019.

[31] Peczak P, Luton MJ. The effect of nucleation models on dynamic recrystallization: I. Homogeneous stored energy distribution. Phil Mag B 1993;68:115–44. http://dx.doi.org/10.1080/13642819308215285.

[32] Gourdet S, Montheillet F. A model of continuous dynamic recrystallization. Acta Mater 2003;51(9):2685–99. http://dx.doi.org/10.1016/S1359-6454(03)00078-8.

[33] Montheillet F, Lurdos O, Damamme G. A grain scale approach for modeling steady-state discontinuous dynamic recrystallization. Acta Mater 2009;57(5):1602–12. http://dx.doi.org/10.1016/j.actamat.2008.11.044.

[34] Nagra JS, Brahme A, Lévesque J, Mishra R, Lebensohn RA, Inal K. A new micromechanics based full field numerical framework to simulate the effects of dynamic recrystallization on the formability of HCP metals. Int J Plast 2020;125:210–34. http://dx.doi.org/10.1016/j.ijplas.2019.09.011.

[35] Xu B, Qu J, Jin Q. Deformation behaviour of the hot upsetting cylindrical specimen with dynamic recrystallization. Int J Mech Sci 2006;48(2):190–7. http://dx.doi.org/10.1016/j.ijmecsci.2005.08.010.

[36] Zeng Z, Jonsson S, Roven HJ, Zhang Y. Modeling the flow stress for single peak dynamic recrystallization. Mater Des 2009;30(6):1939–43. http://dx.doi.org/10.1016/j.matdes.2008.09.004.

[37] Qian M, Guo ZX. Cellular automata simulation of microstructural evolution during dynamic recrystallization of an HY-100 steel. Mater Sci Eng A 2004;365:180–5. http://dx.doi.org/10.1016/j.msea.2003.09.025.

[38] Ding R, Guo ZX. Coupled quantitative simulation of microstructural evolution and plastic flow during dynamic recrystallization. Acta Mater 2001;49:3163–75, URL: www.elsevier.com/locate/actamat.

[39] Hallberg H. Approaches to modeling of recrystallization. Metals 2011;1(1):16–48. http://dx.doi.org/10.3390/met1010016.

[40] Peczak P. A monte carlo study of influence of deformation temperature on dynamic recrystallization. Acta Metall Mater 1995;43:1279–91. http://dx.doi.org/10.1016/0956-7151(94)00280-U.

[41] Borodin EN, Morozova A, Bratov V, Belyakov A, Jivkov AP. Experimental and numerical analyses of microstructure evolution of Cu-Cr-Zr alloys during severe plastic deformation. Mater Charact 2019;156:109849. http://dx.doi.org/10.1016/j.matchar.2019.109849.

[42] Zhu S, Borodin E, Jivkov AP. Topological phase transitions of grain boundary networks during severe plastic deformations of copper alloys. Acta Mater 2023. http://dx.doi.org/10.1016/j.actamat.2023.119290.

[43] Borodin EN, Jivkov AP. Evolution of triple junctions' network during severe plastic deformation of copper alloys–a discrete stochastic modelling. Phil Mag 2020;100(4):467–85. http://dx.doi.org/10.1080/14786435.2019.1695071.

[44] Zhu S, Borodin E, Jivkov AP. Triple junctions network as the key pattern for characterisation of grain structure evolution in metals. Mater Des 2021;198:109352. http://dx.doi.org/10.1016/j.matdes.2020.109352.

[45] Kozlov D. Combinatorial algebraic topology. Springer; 2008.

[46] Bushuev O. Source code for DDRX simulations. 2024, URL: https://github.com/PRISBteam/ddrx-simulation.

[47] Bushuev O. Polyhedral cell complex (PCC) analyser code. 2022, URL: https://github.com/PRISBteam/Voronoi_PCC_Analyser.

[48] Quey R. Neper. 2022, URL: https://neper.info/index.html.

[49] Mishra A, Martin M, Thadhani N, Kad B, Kenik E, Meyers M. High-strain-rate response of ultra-fine-grained copper. Acta Mater 2008;56(12):2770–83. http://dx.doi.org/10.1016/j.actamat.2008.02.023.

[50] Qian LY, Fang G, Zeng P, Wang Q. Experimental and numerical investigations into the ductile fracture during the forming of flat-rolled 5083-O aluminum alloy sheet. J Mater Process Technol 2015;220:264–75. http://dx.doi.org/10.1016/j.jmatprotec.2015.01.031.

[51] Ansys LS Dyna solver. 2023, URL: https://lsdyna.ansys.com.

[52] Jivkov AP, Berbatov K, Boom PD, Hazel AL. Microstructures, physical processes, and discrete differential forms. Procedia Struct Integr 2023;43:15–22. http://dx.doi.org/10.1016/j.prostr.2022.12.228.

[53] Boom PD, Kosmas O, Margetts L, Jivkov AP. A geometric formulation of linear elasticity based on discrete exterior calculus. Int J Solids Struct 2022;236–237:111345. http://dx.doi.org/10.1016/j.ijsolstr.2021.111345.

[54] Berbatov K, Boom PD, Hazel AL, Jivkov AP. Diffusion in multi-dimensional solids using Forman's combinatorial differential forms. Appl Math Model 2022;110:172–92. http://dx.doi.org/10.1016/j.apm.2022.05.043.

[55] Borodin E, et al. MATERiA project. 2024, URL: http://materia.team.

[56] Frary ME, Schuh CA. Correlation-space description of the percolation transition in composite microstructures. Phys Rev E 2007;76(4). http://dx.doi.org/10.1103/PhysRevE.76.041108.

[57] Borodin E. Polyhedral cell complex (PCC) processing design code. 2023, URL: https://github.com/PRISBteam/PCC_Processing_Design.

[58] Panzarino JF, Pan Z, Rupert TJ. Plasticity-induced restructuring of a nanocrystalline grain boundary network. Acta Mater 2016;120:1–13. http://dx.doi.org/10.1016/j.actamat.2016.08.040.

[59] Gutkin M, Mikaelyan K, Ovid'ko I. Athermal grain growth through cooperative migration of grain boundaries in deformed nanomaterials. Scr Mater 2008;58(10):850–3. http://dx.doi.org/10.1016/j.scriptamat.2008.01.002.

[60] Frary M, Schuh CA. Connectivity and percolation behaviour of grain boundary networks in three dimensions. Phil Mag 2005;85(11):1123–43. http://dx.doi.org/10.1080/14786430412331323564.

[61] Shannon CE. A mathematical theory of communication. Bell Syst Tech J 1948;27(3):379–423. http://dx.doi.org/10.1002/j.1538-7305.1948.tb01338.x.

[62] Borodin E, et al. MATERiA project. 2024, URL: https://materia.team/assets/simulations/DDRX.html.

[63] Mayer AE, Khishchenko KV, Levashov PR, N. MP. Modeling of plasticity and fracture of metals at shock loading. J Appl Phys 2013;113:193508. http://dx.doi.org/10.1063/1.4805713.

[64] song Dai Q, lai Deng Y, guo Tang J, Wang Y. Deformation characteristics and strain-compensated constitutive equation for AA5083 aluminum alloy under hot compression. Trans Nonferr Met Soc China 2019;29(11):2252–61. http://dx.doi.org/10.1016/S1003-6326(19)65131-9.

[65] Fan XH, Li M, Li DY, Shao YC, Zhang SR, Peng YH. Dynamic recrystallisation and dynamic precipitation in AA6061 aluminium alloy during hot deformation. Mater Sci Technol 2014;30(11):1263–72. http://dx.doi.org/10.1179/1743284714Y.0000000538.

[66] Krasnikov V, Mayer A. Modeling of plastic localization in aluminum and Al–Cu alloys under shock loading. Mater Sci Eng A 2014;619:354–63. http://dx.doi.org/10.1016/j.msea.2014.09.105.

[67] Borodin EN, Mayer AE. Structural model of mechanical twinning and its application for modeling of the severe plastic deformation of copper rods in Taylor impact tests. Int J Plast 2015;74:141–57. http://dx.doi.org/10.1016/j.ijplas.2015.06.006.

[68] Kuhn H, Medlin D. ASM handbook. Volume 8: Mechanical testing and evaluation. Materials Park, OH 44073-0002, USA: ASM International, Member/Customer Service Center; 2000, p. 998, 2000.

[69] Wang P, Jiang H, Xu S, Shi C, Shan J, Zhang M, Liu Y, Lu D, Hu S. Dynamic plastic instability of ring-shaped aluminum alloy with different interface behaviors. Int J Impact Eng 2021;155:103898. http://dx.doi.org/10.1016/j.ijimpeng.2021.103898.

[70] Hallquist JO, et al. LS-DYNA keyword user's manual. Vol. 970, Livermore Software Technology Corporation; 2007, p. 299–800, URL: https://www.dynasupport.com/manuals/ls-dyna-manuals.

[71] Venkatesan J, Iqbal M, Gupta N, Bratov V, Kazarinov N, Morozov F. Ballistic characteristics of bi-layered armour with various aluminium backing against ogive nose projectile. Procedia Struct Integr 2017;6:40–7. http://dx.doi.org/10.1016/j.prostr.2017.11.007.

[72] Rai R, Kumar G, Dagar S, Somashekar V, Mboreha CA, Modi P. Numerical simulation of ballistic impact on aluminium 5083-H116 plate with Johnson Cook plasticity model. Mater Today: Proc 2021;46:10619–27. http://dx.doi.org/10.1016/j.matpr.2021.01.373.

[73] Lukyanov AA. Constitutive behaviour of anisotropic materials under shock loading. Int J Plast 2008;24(1):140–67. http://dx.doi.org/10.1016/j.ijplas.2007.02.009.

[74] Taylor GI, Quinney H. The latent energy remaining in a metal after cold working. Proc R Soc A 1934;143(849):307–26. http://dx.doi.org/10.1098/rspa.1934.0004.

[75] Rittel D, Zhang L, Osovski S. The dependence of the Taylor–Quinney coefficient on the dynamic loading mode. J Mech Phys Solids 2017;107:96–114. http://dx.doi.org/10.1016/j.jmps.2017.06.016.

[76] Bragov A, Konstantinov A, Lomunov A, Sergeichev I, Fedulov B. Experimental and numerical analysis of high strain rate response of Ti-6Al-4V titanium alloy. J Physique IV 2009;137:1465. http://dx.doi.org/10.1051/dymat/2009207.

[77] Kolsky H. An investigation of the mechanical properties of materials at very high rates of loading. Proc Phys Soc Sect B 1949;62(11):676. http://dx.doi.org/10.1088/0370-1301/62/11/302.

[78] Li YS, Zhang Y, Tao NR, Lu K. Effect of the Zener-Hollomon parameter on the microstructures and mechanical properties of Cu subjected to plastic deformation. Acta Mater 2009;57:761–72. http://dx.doi.org/10.1016/j.actamat.2008.10.021.